

AERODYNAMIC EFFECT OF PITCHING MOTION FOR FLAPPING AIRFOIL ACROSS DIFFERENT SWEEPING TRAJECTORIES

Yichi Liu [1] , Bifeng Song [1] ,Libing Zhou [1]

[1] School of Aeronautics, Northwestern Polytechnical University, Xi'an 710129, Shaanxi, China

Abstract

Leading-edge pitching effectively improves the thrust performance of flapping airfoils, and its underlying aerodynamic mechanisms differ notably under various plunging-sweeping motion trajectories.This paper numerically investigates the aerodynamic performance, focusing on thrust characteristics and propulsive efficiency, of a flapping airfoil under coupled pitching, plunging, and sweeping motions. The numerical method is first validated using the plunging motion of a NACA 0012 airfoil.The GOE 9K airfoil, representative of bird outer-wing geometry, is adopted as the computational model. The effects of pitching amplitude α_m on the time-averaged thrust coefficient and propulsive efficiency are systematically analyzed under different surging-to-plunging amplitude ratios X_m/Y_m, with particular attention paid to the cruising elliptical trajectory at φ_1=90°.By examining vortex evolution and effective flow parameters, the underlying mechanisms of aerodynamic regulation by pitching motion are elucidated. The results show that moderate pitching amplitude (24° to 28°) optimizes thrust by enhancing upstroke leading-edge vortex strength, while excessive pitching (≥40°) induces full-cycle drag. An asymmetric pitching ratio $\alpha_{up}/\alpha_{down}$ =0.4 maximizes thrust, and 0.8 yields optimal efficiency. The conclusions clarify the regulation mechanism of pitching amplitude on aerodynamic performance during cruising flight. This work not only deepens the understanding of avian flight aerodynamics,but also provides practical references for the kinematic optimization of bionic flapping-wing micro air vehicles (MAVs).

Keywords: Aerodynamics; Pitching Motion; Plunging-Sweeping Trajectories

1. Introduction

Over hundreds of millions of years, birds have evolved remarkable flight capabilities to forage, evade predators, and reproduce, with their flapping wings delivering excellent aerodynamic performance[1]. Exploring the aerodynamic effects of diverse flapping motions is vital to uncover avian flight mechanisms and guide flapping-wing aircraft design.

Unlike conventional fixed-wing aircraft, bird wings serve as the direct source of both lift and thrust. Katzmayr[2] verified the Knoller-Betz effect, demonstrating that variations in effective angle of attack induced by two-dimensional airfoil plunging generate a streamwise lift component, thereby producing lift and thrust simultaneously. In reality, bird wing kinematics are far more intricate, encompassing flapping, pitching, sweeping, and folding motions coordinated by skeletal articulation. In existing research, flapping and sweeping are commonly simplified as vertical plunging and horizontal oscillation of two-dimensional airfoils, and extensive investigations have been conducted on coupled plunging-sweeping motion. Biological flight adopts asymmetric wingbeat cycles with shorter downstroke durations to augment thrust and lift[3]. Sweeping motion enhances thrust and efficiency when paired with forward sweep during the downstroke and backward sweep during the upstroke, albeit with a slight reduction in lift[4]. Koekkoek[5] found that the angle between the flapping plane and

horizontal significantly modulates leading-edge vortex structures, highlighting sweeping's vital role in lift generation during flapping flight. Related studies also reveal that rational flapping-sweeping coordination improves energy extraction efficiency, while optimal phase difference and amplitude ratio substantially enhance lift performance[6,7,8].

Nevertheless, these studies have not systematically addressed the aerodynamic impact of airfoil pitching. During level flapping flight, chordwise rotation about the leading edge of feathered regions arises from both active shoulder control and passive aerodynamic/muscular effects[9,10]. It has been confirmed that the outer wing contributes more significantly to thrust than the inner wing, with larger pitching and flapping-sweeping amplitudes in the outer segment. Thus, neglecting pitching effects across different motion trajectories is unreasonable. Prior work found that pitching regulates dynamic stall by altering leading-edge vortex evolution, thereby influencing lift generation[11,12]. Meanwhile, pitching exerts a pronounced effect on thrust: the time-averaged thrust coefficient rises with pitching reduced frequency and amplitude, while excessive pitching degrades propulsive efficiency[13]. A 90° phase difference between pitching and plunging is identified to optimize propulsion efficiency[14].

In summary, current research on bird wing pitching and plunging-sweeping motion remains fragmented. Limited attention has been paid to spanwise variations in airfoil geometry and the aerodynamic effects of pitching under diverse trajectories. Specifically, the influence of outer-wing pitching on thrust performance across varying motion paths has yet to be fully explored.

To address these gaps, this paper selects the GOE 9K airfoil as the computational model. The aerodynamic performance, focusing on thrust characteristics, of coupled pitching-plunging-sweeping motion is systematically investigated. The effects of pitching amplitude α_m on time-averaged thrust coefficient and propulsive efficiency under different X_m/Y_m ratios are analyzed, with focus on the cruising elliptical trajectory at a phase difference of 90°. By examining vortex structures and kinematic parameters, pitching's aerodynamic regulation mechanism is clarified. This work aims to reveal pitching's thrust modulation during pigeon cruising flight. The findings advance avian aerodynamic understanding and guide bio-inspired flapping-wing vehicle kinematic design.

2. Methodology

2.1. Geometric model and flapping motion

The static geometric configuration of avian wings is characterized by their planar morphology and cross-sectional airfoil profiles, shown in Fig. 1. This study utilizes the GOE 9K airfoil as the computational model, with its geometric airfoil shown in Fig. 2. The GOE9K airfoil features a sharp leading edge and a flat, thin profile, demonstrating close geometric similarity to the distal wing sections of avian species.

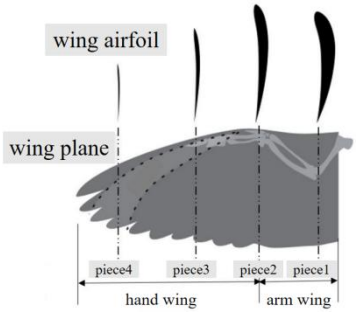


Fig. 1 The typical planar shape of bird wings and the cross-sectional shapes at different positio

ns along the wingspan direction[1]

Fig. 2 GOE 9K airfoil

The kinematic of flapping airfoil combines a plunging motion in the vertical direction $y(t)$, a pitching motion about the leading edge point $\alpha(t)$, and a surging motion in the horizontal direction $x(t)$ .The kinematic synchronization of avian wings during flight is governed by identical flapping frequencies in both vertical and horizontal directions. Consequently, this study employs a unified frequency parameter to model the coupled plunging, sweeping, and pitching motions. The kinematic equations of different motions are defined as:

$$\begin{cases} y(t) = Y_m \cos(2\pi f \cdot t) \\ \alpha(t) = \alpha_0 + \alpha_m \cos(2\pi f \cdot t + \varphi_0) \\ x(t) = X_m \cos(2\pi f \cdot t + \varphi_1) \end{cases} \tag{1}$$

where Y_m is the plunging amplitude, α_0 is the mean pitching angle, α_m is the pitching amplitude, X_m is the surging amplitude, and f represents the flapping frequency. Furthermore, φ_0 is the phase difference between pitching motion and plunging motion. φ_1 represents the phase difference between surging motion and plunging motion.

φ_1 can adjust the motion trajectory of flapping airfoils.X_m/Y_m is used to adjust the stroke angle of each trajectory. Correspondingly, the schematic diagrams of motion trajectories with different combinations of φ_1 and X_m/Y_m are shown in Fig. 3.

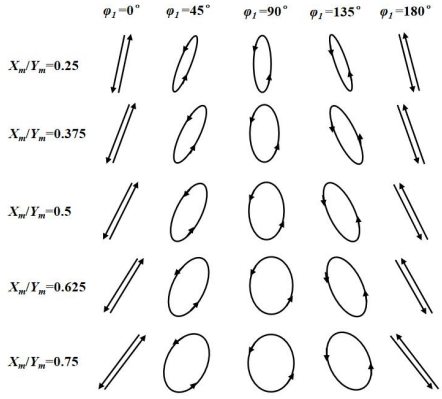


Fig. 3 Motion trajectories under different φ_1 and X_m/Y_m

φ_0 and α_m critically govern the instantaneous angle between the airfoil chord line and free-stream direction, with α_0 effectively serving as the initial angle of attack.

The reduced frequency k, which quantifies the unsteady characteristics of flapping-wing motion, is defined in Eq. (2). The detailed kinematic parameter values adopted in this study are systematically tabulated in Table 1.

$$k = \frac{\omega c}{2U_\infty} \tag{2}$$

where ω denotes the flapping angular frequency,$\omega = 2\pi f$; c represents the reference chord length ($c = 0.1\text{m}$ in this study); $U_\infty$is the free-stream velocity.

Table 1 Values of kinematic parameters for flapping motion

Parameter	Y_m/c	α_0	α_m	φ_0	X_m/c	φ_1	k	U_∞
Value	2.0	10°	0°/ 24~44°	90°	0~1.5	0~180°	0.2513	10m/s

2.2. Performance evaluation

The aerodynamic performance of flapping wings is evaluated using cycle-averaged

coefficients of lift $C_{L,mean}$, thrust $C_{T,mean}$, power consumption $C_{P,mean}$, and propulsion efficiency η_T, defined as follows:

$$C_{L,mean} = \frac{\frac{1}{T}\int_t^{t+T} F_y(t)dt}{0.5\rho U_\infty^2 S} = \frac{1}{T}\int_t^{t+T} C_L dt \tag{3}$$

$$C_{T,mean} = \frac{\frac{1}{T}\int_t^{t+T} -F_x(t)dt}{0.5\rho U_\infty^2 S} = \frac{1}{T}\int_t^{t+T} C_T dt \tag{4}$$

$$C_{P,mean} = \frac{\frac{1}{T}\int_t^{t+T} P_{input}(t)dt}{0.5\rho U_\infty^3 S} = \frac{1}{T}\int_t^{t+T} C_P dt \tag{5}$$

where $F_y(t)$ and $F_x(t)$ are the instantaneous forces in y-direction and x-direction at time t, C_L and C_T are the corresponding non-dimensional coefficients. The instantaneous consumed power P_{input} and its coefficient C_P can be expressed as Eqs.(6) and (7)。, where C_{Py}, C_{Px}, and $C_{P\alpha}$ represent the power coefficients consumed by plunging motion, surging motion, and pitching motion, respectively.

$$P_{input} = F_y(t)\frac{dy(t)}{dt} + F_x(t)\frac{dx(t)}{dt} + M(t)\frac{d\alpha(t)}{dt} \tag{6}$$

$$C_P = C_{Py} + C_{Px} + C_{P\alpha} = \frac{1}{U_\infty}(C_L\frac{dy(t)}{dt} - C_T\frac{dx(t)}{dt} + C_M\frac{d\alpha(t)}{dt}) \tag{7}$$

Propulsive efficiency can be defined as follows:

$$\eta_T = \frac{C_{T,mean}}{C_{P,mean}} \tag{8}$$

The effective angle of attack α_{eff} and effective inflow velocity u_{eff} are defined to characterize the unsteady kinematics and localized flow dynamics during flapping motion. As shown in Fig. 5, u_{eff} represents the resultant velocity combining the free-stream velocity and the induced velocity from wing motion. α_{eff} is the angle between the chord line of airfoil and the resultant flow velocity.Using the mid-chord point as the reference, these parameters are formally expressed as Eqs. (9) and (10)

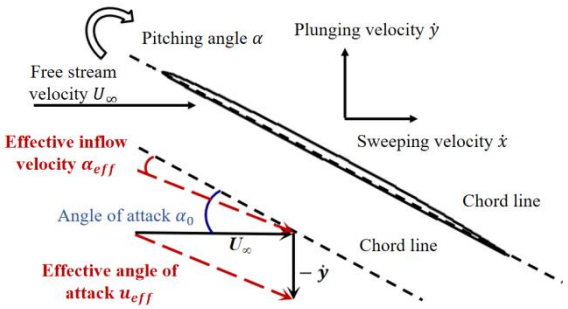


Fig. 4 Effective angle of attack α_{eff} and effective inflow velocity u_{eff}

$$u_{eff}(t) = \sqrt{(U_\infty - \dot{x}(t) + \sin(\alpha)\,\dot{\alpha}(t)c/2)^2 + (\dot{y}(t) - \cos(\alpha)\,\dot{\alpha}(t)c/2)^2} \tag{9}$$

$$\alpha_{eff}(t) = \alpha(t) + \arctan(\frac{-\dot{y}(t) + \cos(\alpha)\,\dot{\alpha}(t)c/2}{U_\infty - \dot{x}(t) + \sin(\alpha)\,\dot{\alpha}(t)c/2}) \tag{10}$$

2.3. Numerical methods and solver validation

An in-house CFD solver, called “PMNS2D”, [15,16,17] is used in this work. The preconditioned Unsteady Reynolds Averaged Navier-Stokes (URANS) equations are solved based on a Finite Volume Method (FVM) within the framework of an efficient Full Approximation Storage (FAS) multigrid method. The space discretization is a cell-centered finite volume method using central difference, with nearly second-order accuracy on smooth structured grid. A dual time-stepping method is adopted for time marching and the LU-SGS scheme is implemented to accelerate the convergence for the inner iteration of pseudo-time stepping. SA turbulence

model is adopted in this study to close the URANS equations.

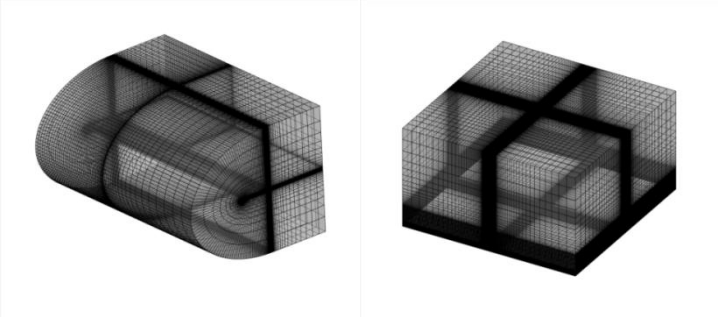
This case employs the experimental results of Heathcote[18] on plunging motion of an NACA 0012 flapping wing in a water tunnel to validate the accuracy of the numerical simulation method under identical Reynolds number and kinematic parameters.

The plunging motion is defined as:

$$H(\mathrm{t}) = H_1 \cos(\omega t) \tag{11}$$

where H_1 is the plunging amplitude and ω is the radial frequency of the plunging motion.

A rectangular flapping wing with an NACA0012 airfoil section, featuring an aspect ratio of 6 is tested in this case.The flow conditions are listed as follows: free-stream velocity U_∞ =4.4m/s, the chord-based Reynolds number *Re*=3× 10^4 . The plunging amplitude are H_1=0.175m, and the radial frequency of the plunging motion ω=10.92rad/s. The distribution of the computational grids are shown in Fig. 5, including background grid(a) with about 1.12 million cells and wing grid(b) with about 0.76 million cells, the first grid layer spacing is 5.4×10^{-4}c, and y+ is less than 1.0.



(a)Wing grid (b)Background grid

Fig. 5 Wing grid and background grid

The periodic thrust coefficients from the current computational study are compared with experimental data from Heathcote's water tunnel tests in Fig. 6. Generally good agreement is observed between the numerical predictions ("Example") and experimental measurements across most phase angles.A minor discrepancy is identified near the thrust trough (phase ≈ 180°), where the computational results are found to deviate slightly from experimental values. This phase-specific variation is further investigated through reference to the numerical simulations by Liu et al.[19] ("Cal by Liu"). The consistency between our computational results and Liu's predictions is confirmed, demonstrating that the observed trough discrepancy is attributed to inherent flow physics rather than algorithmic deficiencies.

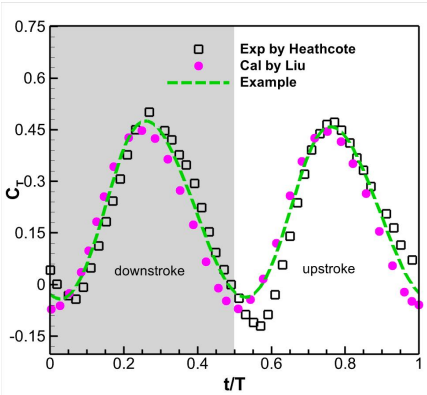


Fig. 6 Comparison of thrust coefficient between experiment and CFD simulations

2.4. Convergence study of grid size and time resolution

In this part, different grid sizes and time steps are adopted to choose a suitable mesh scale and time step for good accuracy of numerical simulation. The flow conditions are free-stream velocity U_∞=10m/s, Reynolds number Re =6.8×10^4, which are quite similar to that of a pigeon's flight during cruising. The kinematic parameters of flapping motion have been shown in Table 1, with X_m=0 adopted in this section.

Table 2 Values of kinematic parameters for flapping motion

Parameter	Y_m/c	α_0	α_m	φ_0	X_m/c	φ_1	k
Value	1.0	8°	12°	90°	0	0°	0.2513

2.4.1. Grid resolution study

Three grid systems with varying levels (coarse/medium/dense) are implemented for grid independence verification, with geometric specifications detailed in Table 3. All airfoils employ C-type topology, featuring 20-chord-length far-field extensions (20c) to eliminate boundary interference effects.The medium-level grid for GOE9K airfoil is illustrated in Fig. 7.

Table 3 Parameters of different grids employed for GOE 9K airfoil

Parameter	Far field radius/c	Grid size	First layer spacing/c	Spacing increasing ratio
Coarse grid	20	389×85	3.0×10^{-4}	1.01
Medium grid	20	489×133	2.0×10^{-4}	1.01
Dense grid	20	629×209	1.0×10^{-4}	1.01

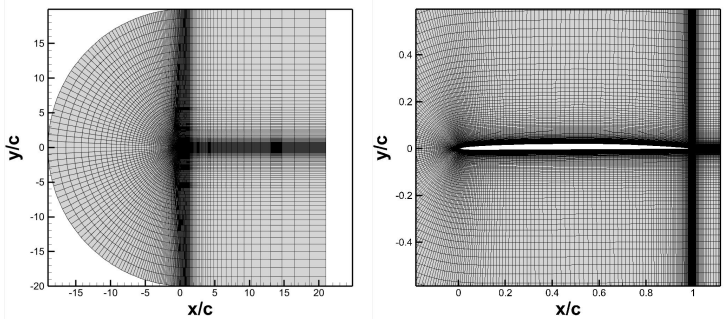
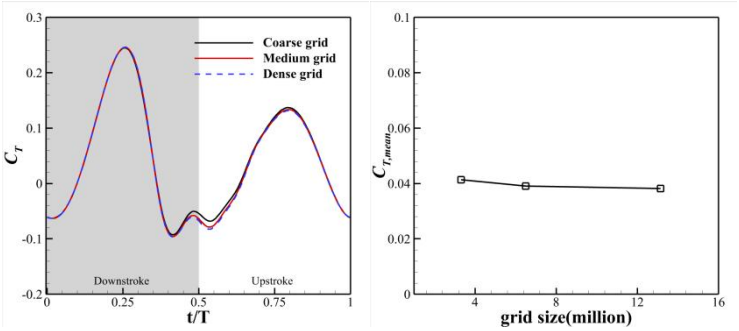


Fig. 7 Medium-sized GOE 9K airfoil C-grid

As shown in Fig. 8, the instantaneous thrust coefficient profiles from medium and fine grids demonstrate virtually identical trends, while their time-averaged values exhibit merely 0.97% relative deviation. This quantitatively confirms that grid density exerts negligible effects on computational accuracy, thereby satisfying grid independence criteria. Consequently, all subsequent numerical simulations in this study are conducted using the medium-density grid configuration.



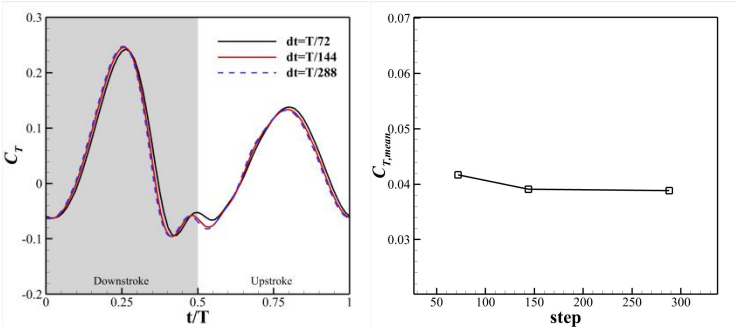
(a)C_T (b)$C_{T,mean}$

Fig. 8 Instantaneous thrust coefficient and time-averaged thrust coefficient for different

grid sizes

2.4.2. Time resolution study

Unsteady simulation is performed with a flapping cycle divided into 144, 288, and 432-time steps. Each case is calculated for 10 cycles to ensure convergence of results. Fig. 9 shows that the instantaneous thrust coefficient profiles with 144 and 288 time steps per computational cycle achieve virtually identical trajectories, while their time-averaged values show merely 0.71% relative variation. Good time resolution can be achieved with 288-time steps in a flapping cycle. Hence, 144-time steps during a cycle are adopted to carry out all the subsequent simulations.



(a)C_T (b)$C_{T,mean}$

Fig. 9 Instantaneous thrust coefficient and time-averaged thrust coefficient for different time steps

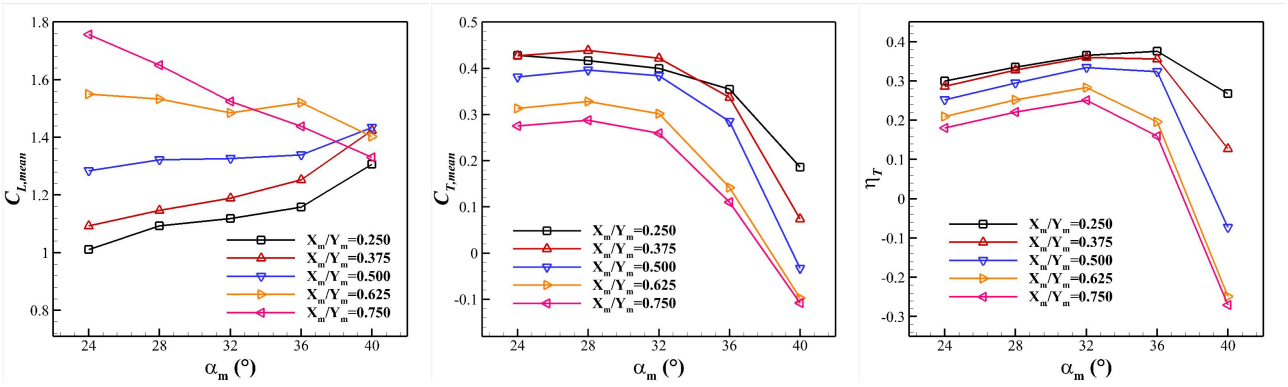
3. Results and discussion

3.1. Effects of α_m under different X_m/Y_m

The motion trajectory at φ_1=90° is elliptical, closely resembling the outer-wing kinematics of pigeons during cruising flight[17]. This section systematically analyzes the aerodynamic performance and underlying flow mechanisms of the flapping airfoil under coupled pitching and plunging-sweeping motions, focusing on the effects of pitching amplitude α_m and amplitude ratio X_m/Y_m.

As illustrated in Fig. 10(a), the $C_{L,mean}$ is observed to increase gradually with X_m/Y_m when $X_m/Y_m \leq$0.500, but exhibits a decreasing trend when $X_m/Y_m >$ 0.500. The maximum $C_{L,mean}$ of 1.757 is achieved at X_m/Y_m=0.750 with α_m=24°, though this represents a 3.83% reduction compared to the non-pitching configuration.

Fig. 10(b) demonstrates that $C_{T,mean}$ generally follow a parabolic trend with increasing α_m across all X_m/Y_m values. The peak $C_{T,mean}$ of 0.69 is recorded at X_m/Y_m=0.375 with α_m=28°.

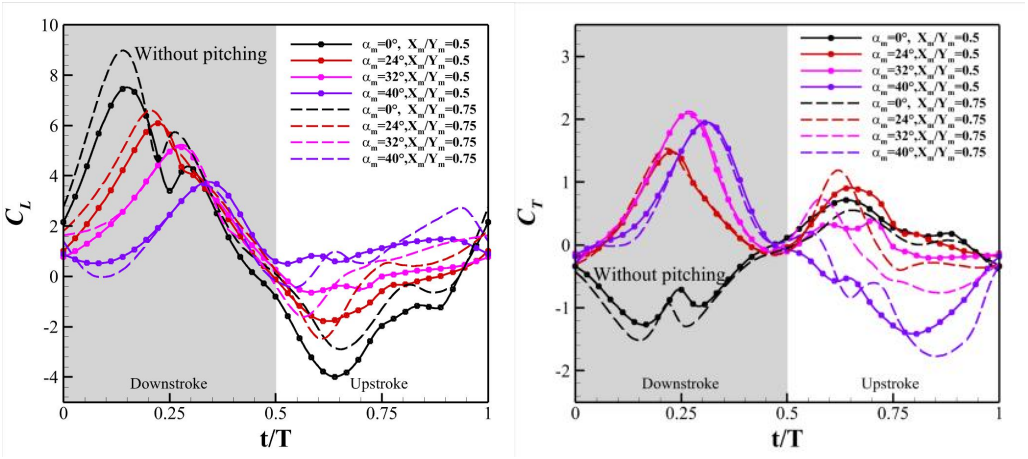


(a)$C_{L,mean}$ (b)$C_{T,mean}$ (c)η_T

Fig. 10 Effects of α_m on $C_{L,mean}$、$C_{T,mean}$、η_T under different X_m/Y_m when φ_1=90°

As shown in Fig. 10(c), the η_T first increases steadily and then decreases sharply with increasing pitching angle across the X_m/Y_m range.

The $C_{L,mean}$ exhibits different trends with α_m variation under different X_m/Y_m. Selected cases of X_m/Y_m=0.500 and X_m/Y_m=0.750 are analyzed.

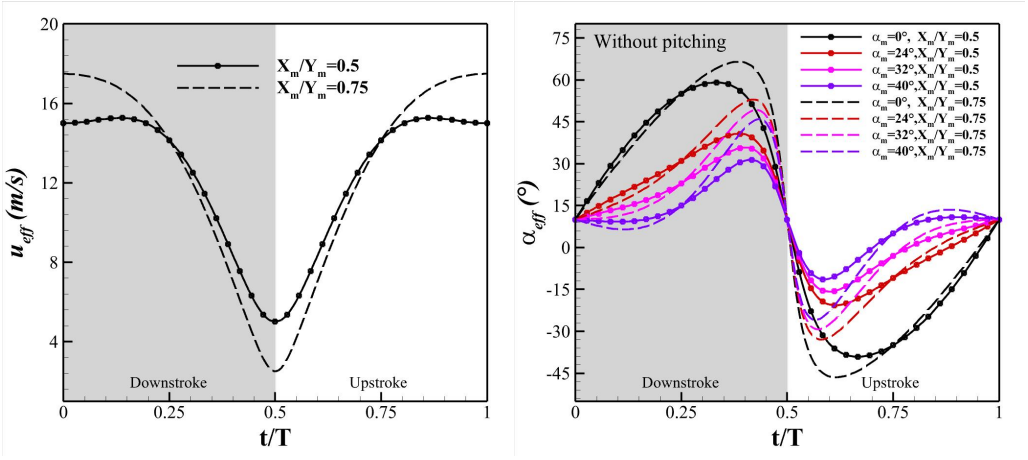


(a)C_L (b)C_T

Fig. 11 Instantaneous thrust coefficient and power coefficient during a flapping cycle for different α_m when φ_1=90°

As shown in Fig. 11(a), the peak C_L of the non-pitching airfoil is recorded at 0.125T when α_m=0°, with its negative peak observed at 0.650T. With increasing α_m, delayed positive peak timing and advanced negative peak timing are accompanied by reduced peak magnitudes. The differences in C_L and C_T during downstroke caused by X_m/Y_m increments are demonstrated to diminish with larger α_m. When φ_1 =90°, modified $C_{L,mean}$ variations are primarily achieved through amplified negative lift peaks during upstroke.

Fig. 11(b) indicates that the C_T of non-pitching configurations is slightly reduced with increased X_m/Y_m. For pitching airfoils, downstroke C_T remain minimally affected, while upstroke C_T peaks are enhanced and advanced. In comparison to φ_1 =0°, there is no statistically significant distinctions in downstroke C_T patterns, with all observable variations concentrated in the upstroke phase when φ_1=90°.



(a)u_{eff} (b)α_{eff}

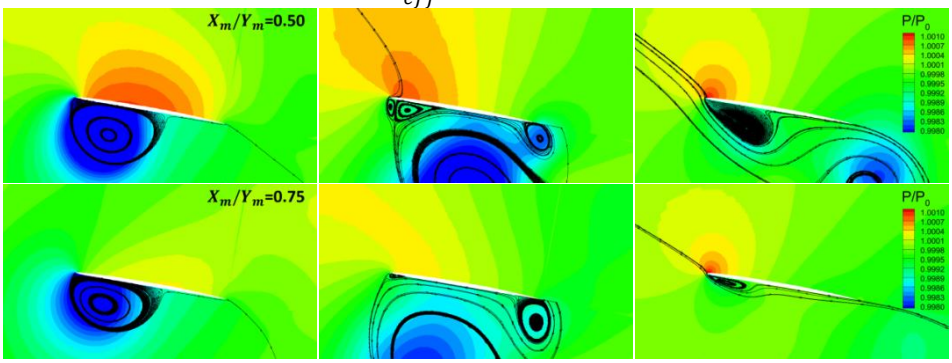
Fig. 12 Change of u_{eff} and α_{eff} under different X_m/Y_m when φ_1=90°

As illustrated in Fig. 12, increased X_m/Y_m reduce u_{eff} while amplifying absolute α_{eff} during the initial upstroke phase, with reversed trends observed in the latter phase where u_{eff} rises and absolute α_{eff} diminishes. Elevated α_m generally decrease absolute α_{eff} magnitudes

throughout the upstroke cycle.

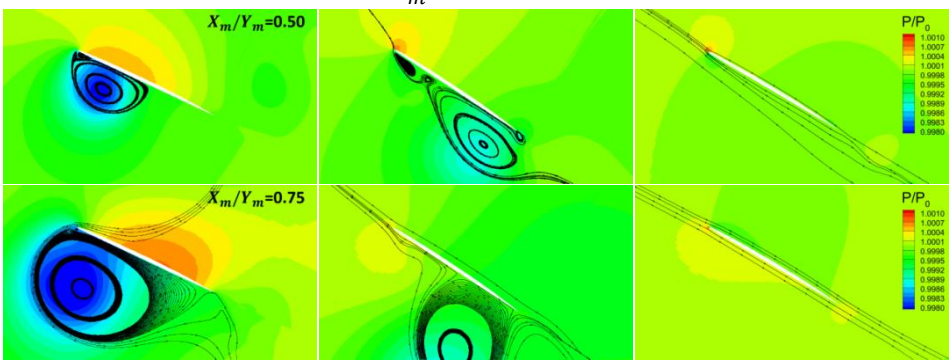
For non-pitching airfoils, Fig. 13(1) demonstrates that X_m/Y_m increments minimally alter LEV(Leading Edge Vortex) structures during early upstroke. The pressure differential reduction between upper and lower surfaces is primarily attributed to diminished u_{eff} rather than structural modifications. During late upstroke, the reduced α_{eff} induces delayed LEV formation, accompanied by contracted low-pressure regions on the lower surface, ultimately resulting in diminished thrust components.

For pitching airfoils, Fig. 13(2)(3) demonstrates that at α_m=24°, absolute α_{eff} magnitudes are rapidly increased by X_m/Y_m elevation during early upstroke, which is followed by enhanced lower-surface LEV development and augmented leading-edge suction. However, rapid LEV decay and detachment are induced by excessive α_{eff} values, resulting in reduced pressure differentials. During late upstroke, upward pressure differentials are amplified by increased u_{eff}, with thrust components being paradoxically diminished.When α_m=40°, net drag is manifested by pressure differential components throughout the cycle.The peak absolute α_{eff} magnitudes are elevated by X_m/Y_m increments during early upstroke, while drag reduction is observed. This improvement is attributed to pressure differential reductions caused by diminished u_{eff} rather than LEV - related mechanisms. Similarly during late upstroke, LEV structures on the upper surface remain unaffected, where drag increments are generated through pressure differential amplifications associated with increased u_{eff}.



（a）0.625T （b）0.750T （c）0.875T

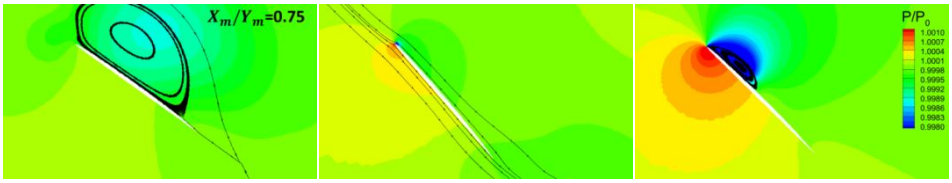
（1）α_m=0°



（a）0.625T （b）0.750T （c）0.875T

（2）α_m=24°





（a）0.625T （b）0.750T （c）0.875T

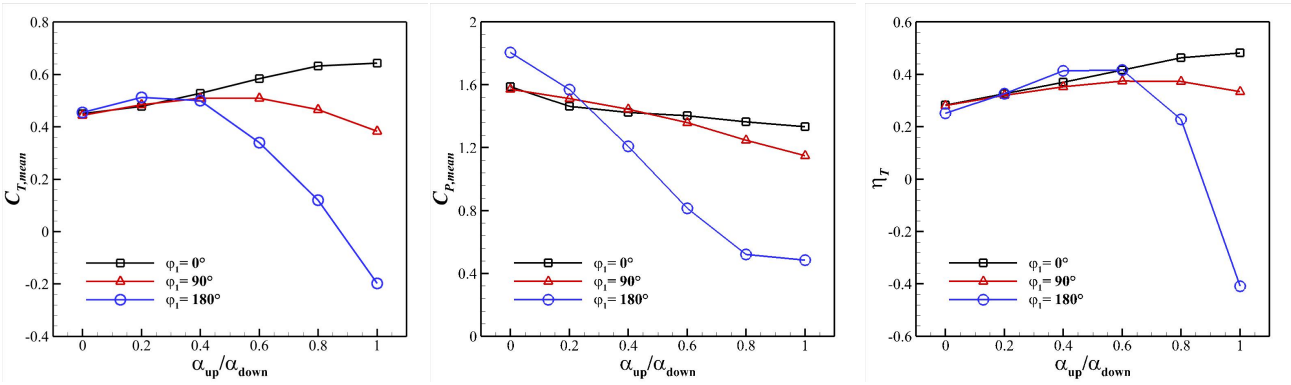
（3）α_m=40°

Fig. 13 Pressure distribution and vortex structure under different α_m during the middle period of upstroke when t=0.625T、0.850T、0.875T

3.2. Mechanisms of $\alpha_{up}/\alpha_{down}$ under different φ_1

The $\alpha_{up}/\alpha_{down}$ is defined as the ratio of the upstroke pitching amplitude to the downstroke pitching amplitude when the durations of upstroke and downstroke phases are equal, with its kinematic formulation provided in Equation (12). The thrust performance dependence on $\alpha_{up}/\alpha_{down}$=0, 0.2, 0.4, 0.6, 0.8 and 1.0 is systematically investigated under three plunging sweep configurations with φ_1=0°, 90° and 180°, while X_m/Y_m =0.5 throughout the parametric study.

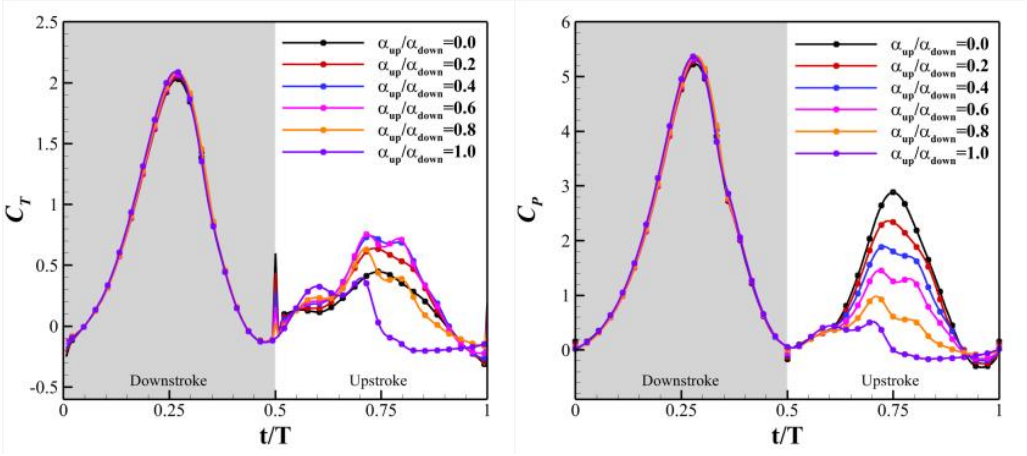
$$\begin{cases} \alpha(t) = \alpha_0 + \alpha_{down}\cos(2\pi f \cdot t + \varphi_0) & 0 \le t < 0.5T \\ \alpha(t) = \alpha_0 + \alpha_{up}\cos(2\pi f \cdot t + \varphi_0) & 0.5T \le t < T \end{cases} \quad (12)$$



(a)$C_{T,mean}$ (b)$C_{P,mean}$ (c)η_T

Fig. 14 Effects of $\alpha_{up}/\alpha_{down}$ on $C_{T,mean}$、$C_{P,mean}$、η_T under different φ_1 when X_m/Y_m=0.5

As shown in Fig. 14, the overall variation trends exhibit similarity with increasing $\alpha_{up}/\alpha_{down}$. Specifically, the $C_{T,mean}$ initially increases then decreases as the $\alpha_{up}/\alpha_{down}$ rises, with higher φ_1 corresponding to lower $\alpha_{up}/\alpha_{down}$ required to reach peak $C_{T,mean}$. The $C_{P,mean}$ demonstrates a continuous reduction with increasing $\alpha_{up}/\alpha_{down}$, while the η_T follows a similar pattern to the thrust coefficient by first increasing then decreasing. This section subsequently analyzes the causal mechanisms through which $\alpha_{up}/\alpha_{down}$ influence $C_{T,mean}$, $C_{P,mean}$, and η_T, supported by time-resolved force coefficient analysis.



(a)C_T (b)C_P

Fig. 15 Instantaneous thrust coefficient and power coefficient during a flapping cycle for different $\alpha_{up}/\alpha_{down}$

The similarity in $C_{T,mean}$ trends across φ_1 leads the current analysis to be focused on φ_1=90° for systematic evaluation of $\alpha_{up}/\alpha_{down}$ effects on C_T and vortical flow structures.As illustrated in Fig. 15, the peak of C_T near the mid-upstroke position is observed to initially intensify then diminish with increasing $\alpha_{up}/\alpha_{down}$, while the aerodynamic power consumption peak during upstroke is progressively reduced. Concurrent temporal advancement of peak occurrences is simultaneously recorded for both parameters throughout the upstroke phase. Maximum thrust generation is attained when $\alpha_{up}/\alpha_{down}$ =0.4, while maximum propulsive efficiency is achieved when $\alpha_{up}/\alpha_{down}$=0.8.

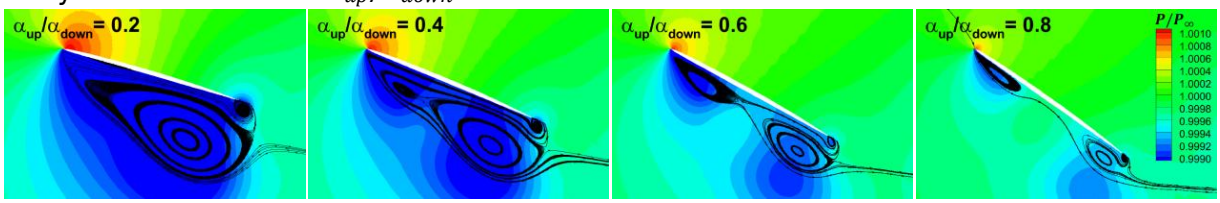


Fig. 16 Pressure distribution and vortex structure under different $\alpha_{up}/\alpha_{down}$ in the middle of upstroke for φ_1=90°

As illustrated in Fig. 16, an increased $\alpha_{up}/\alpha_{down}$ is accompanied by augmented pitching angles at the mid-upstroke phase, with concurrent reduction in LEV intensity being observed to diminish the induced low-pressure region and pressure differential. The thrust peak is characterized by initial enhancement followed by reduction, suggesting that under lower $\alpha_{up}/\alpha_{down}$, thrust improvement is primarily attributed to the projection angle advantage from increased pitching angles exceeding the pressure differential degradation. When higher $\alpha_{up}/\alpha_{down}$ are examined, the accelerated LEV attenuation is found to significantly reduce pressure differential, thereby inducing rapid thrust deterioration. Therefore, controlled reduction of $\alpha_{up}/\alpha_{down}$ can be implemented to achieve enhanced C_T during mid-upstroke operation.

4. Conclusions

This paper numerically investigates the thrust characteristics and underlying aerodynamic mechanisms of a bird outer-wing GOE 9K airfoil under coupled pitching, plunging and sweeping motions. Focusing on the cruising elliptical trajectory at a phase difference of 90°, the effects of pitching amplitude and asymmetric pitching ratio on thrust performance and

propulsive efficiency are systematically analyzed. The main conclusions are as follows:

(1) Under the pigeon-like cruising elliptical trajectory (φ_1=90°), pitching motion is found to exert a dual regulatory effect on thrust. Moderate pitching amplitudes α_m (24° to 28°) are shown to enhance thrust significantly via strengthened upstroke leading-edge vortex development, whereas excessive α_m (≥40°) suppresses vortex evolution and induces net drag over the entire flapping cycle, thereby defining a critical beneficial pitching range for thrust optimization.

(2) The surging-to-plunging amplitude ratio X_m/Y_m is demonstrated to govern the trade-off between lift and thrust, while pitching amplitude α_m dynamically modulates the effective angle of attack α_{eff} and leading-edge vortex evolution. The coupling of these parameters is verified to determine the optimal cruising kinematic parameters, revealing the coordinated aerodynamic mechanism underlying bird outer-wing motion.

(3) The asymmetric pitching ratio is identified to exert a significant influence on thrust performance and propulsive efficiency. Under cruising conditions, the maximum thrust is obtained at $\alpha_{up}/\alpha_{down}$=0.4, and the highest propulsive efficiency is achieved at $\alpha_{up}/\alpha_{down}$=0.8. This result clarifies the aerodynamic rationale for birds' "large downstroke, small upstroke" pitching strategy and provides a direct reference for the kinematic design of bio-inspired flapping-wing vehicles.

(4) Limitations and future work: This study is conducted based on two-dimensional airfoil simulations. Three-dimensional wing models and real wind tunnel tests will be carried out in follow-up research to further verify the conclusions.

5. Copyright Statement

The authors confirm that they, and/or their company or organization, hold copyright on all of the original material included in this paper. The authors also confirm that they have obtained permission, from the copyright holder of any third party material included in this paper, to publish it as part of their paper. The authors confirm that they give permission, or have obtained permission from the copyright holder of this paper, for the publication and distribution of this paper as part of the ICAS proceedings or as individual off-prints from the proceedings.

6. Contact Author Email Address

Yichi Liu: 987210131@qq.com

References

[1] Shen H, Yu Y. Development and key technologies of morphological bionic aircraft [J]. *Advances in Aeronautical Science and Engineering*, 2021, 12(3): 9-19.

[2] Katzmayr, R. Effect of periodic changes of angle of attack on behavior of airfoils [J]. *Legacy CDMS*, 1922, NACA-TM-147.

[3] Chen X, Huang Q, Pan G, Shi Y. Numerical investigation into the time-asymmetry effect on a plunging foil [J]. *Ocean Eng*, 2021, 225: 108833.

[4] Bansmer S E, Radespiel R. Flapping Flight: High Thrust and Propulsive Efficiency due to Forward Gliding Oscillations[J]. *AIAA Journal*, 2012, 50(12): 2937-2942.

[5] Koekkoek G, Muijres F T, Johansson L C, et al. Stroke plane angle controls leading edge vortex in a bat-inspired flapper[J]. *Comptes Rendus*. Mécanique, 2012, 340(1-2): 95-106.

[6] Wu J, Chen Y, Zhao N, Wang T. Influence of stroke deviation on the power extraction performance of a fully-active flapping foil [J]. *Renew Energ*, 2016, 94: 440–51.

[7] Wang B, Zhu B, Zhang W. New type of motion trajectory for increasing the power extraction efficiency of flapping wing devices [J]. *Energy*, 2019, 189: 116072.

[8] Wu Tao. *Aerodynamic mechanism and aerodynamic design optimization of bird-like flapping wing with multi-degree flapping motion* [D]. Northwestern Poly-technical University, 2022.
[9] Shyy W, Berg M, Ljungqvist D. Flapping and flexible wings for biological and micro air vehicles[J]. *Progress in Aerospace Sciences*, 1999, 35(5): 455-505.
[10] Shen Y, Zhang S, et al. Characterization of wing kinematics by decoupling joint movement in the pigeon [J]. *Biomimetics*, 2024, 9: 555.
[11] Ekaterinaris J A, Platzer M F. Computational prediction of airfoil dynamic stall[J]. *Progress in Aerospace Sciences*, 1998, 33(11): 759-846.
[12] Gharali K, Johnson D A. Dynamic stall simulation of a pitching airfoil under unsteady freestream velocity[J]. *Journal of Fluids and Structures*, 2013, 42: 228-244.
[13] Lu K, Xie Y H, Zhang D. Numerical study of large amplitude, nonsinusoidal motion and camber effects on pitching airfoil propulsion[J]. *Journal of Fluids and Structures*, 2013, 36: 184-194.
[14] Koochesfahani M M. Vortical patterns in the wake of an oscillating airfoil[J]. *AIAA Journal*, 1989, 27(9): 1200-1205.
[15] Xie F, Song W, Han Z. Numerical study of high-resolution scheme based on preconditioning method [J]. *J Aircr*, 2009, 46(2): 520–5.
[16] Han Z, He F, Song W, Qiao Z. A preconditioned multi-grid method for efficient simulation of three dimensional compressible and incompressible flows [J]. *Chin J Aeronaut*, 2007, 20(4): 289–96.
[17] Wu T, Song B, Song W, Yang W, Han Z. Aerodynamic performance enhancement for flapping airfoils by co-flowjet [J]. *Chin J Aeronaut*, 2020, 33(10): 2535–54.
[18] Heathcote S, Wang Z, Gursul I. Effect of spanwise flexibility on flapping wing propulsion [J]. *Journal of Fluids and Structures*, 2008, 24: 183–199.
[19] Liu H. Integrated modeling of insect flight: from morphology, kinematics to aerodynamics [J]. *Journal of Computational Physics*, 2009, 228(2): 439-459.